

REPORT TO THE
NATIONAL AERONAUTICS AND SPACE ADMINISTRATION

NASA HEADQUARTERS

STATUS REPORT #8

for

GRANT NAG5-1490

INTERIM
11-46-012
107
80208

**Investigation of Passive Atmospheric Sounding
Using Millimeter- and Submillimeter-Wavelength Channels**

A.J. Gasiewski (principal investigator)

Covering the period from

July 1, 1994 to June 30, 1996

Submitted by:

Professor Albin J. Gasiewski
School of Electrical Engineering
Georgia Institute of Technology
Atlanta, Georgia, 30332-0250
(404) 894-2934 (O) (404) 894-4641 (F)
ag14@prism.gatech.edu

June 25, 1996

NASA Technical Officer:

Dr. Ramesh Kakar
Code EET, B200
NASA Headquarters
Washington, D.C. 20546
(202) 358-0274 (O)
(202) 358-2771 (F)

TABLE OF CONTENTS

I.	INTRODUCTION	1
II.	SUMMARY OF ACTIVITIES	2
III.	CONCLUSIONS AND RECOMMENDATIONS	8
IV.	REFERENCES	23
V.	APPENDIX A	25

INTRODUCTION

This report summarizes progress made during the period from July 1, 1994 through June 30, 1996 on the development of instrumentation and techniques for millimeter- and submillimeter-wave (MMW: 30-300 GHz, and SMMW: 300+ GHz) radiometry for atmospheric sounding purposes. The investigation has focussed on the continued improvement and use of the NASA Goddard Space Flight Center's Millimeter-Wave Imaging Radiometer (MIR) and on MMW and SMMW radiative transfer modeling and retrieval simulation. The MIR is a nine-channel cross track imaging radiometer with channels at 89, 150, $183 \pm 1, \pm 3, \pm 7$, 220, and $325 \pm 1, \pm 3, \pm 9$ GHz. The MIR is a joint project between NASA/GSFC and the Georgia Institute of Technology, with the 325-GHz radiometer having been furnished by Georgia Tech. The MIR has been used in both airborne and ground-based experiments during the above performance period. The primary application of the MIR is to provide calibrated radiometric imagery to verify MMW and SMMW radiative transfer models in clear air, cloud, and precipitation and to develop retrieval techniques using MMW and SMMW channels.

The use of SMMW channels at 325, 380, 424, and 510 GHz offers the possibility of water vapor and temperature sounding at greater spatial resolution than could be obtained at the lower MMW frequencies of 60, 90, 118, 166, 183, and 220 GHz. These channels also can be used to extend the altitude region for which water vapor sounding can be performed up into the lower stratosphere. Together, the use of both SMMW channels and MMW channels are expected to be able to provide additional observational degrees of freedom related to cloud ice particle size.

The MIR imagery has shown that SMMW channels have a uniquely useful degree of sensitivity to thunderstorm anvil clouds, yet do not saturate over clouds as in the case of IR channels. Unlike IR channels, SMMW channels are expected to be able to directly probe the total ice water content of cirrus clouds, a specific capability that would directly benefit observational climatology. Overall, these capabilities are expected to benefit spaceborne sounding of both precipitating cells and non-precipitating clouds, especially in view of the high spatial resolution that can be obtained from spaceborne systems using submillimeter wavelength channels.

SUMMARY OF ACTIVITIES

The goal of this investigation is to develop satellite-based observational techniques for high-resolution imaging of precipitation and sounding of atmospheric cloud ice and water vapor using passive microwave radiometers operating in the frequency range from 89 to approximately 600 GHz. This goal is being achieved by radiative transfer modeling at millimeter-wave and submillimeter-wave frequencies and by the development and operation of an airborne Millimeter-wave Imaging Radiometer (MIR) with channels at 89, 150, 183, 220, and 325 GHz [Racette et al., 1996]. To date, unique millimeter- and submillimeter-wave imagery of the atmosphere has been obtained using the NASA Millimeter-wave Imaging Radiometer (MIR). The MIR was developed jointly by NASA/GSFC and Georgia Tech, and has channels at 89, 150, 183 ± 1 , ± 3 , ± 7 , 220, and 325 ± 1 , ± 3 , ± 9 GHz. These channels sample the radiation field at several of the most important MMW and SMMW tropospheric absorption lines and windows. The MIR imagery over convective stormcells has been used to illustrate the potentially useful cloud and water vapor sensing and stormcell mapping capabilities of SMMW channels [Gasiewski et al., 1994]. The radiometric data has also been used to analyze radiative transfer model discrepancies caused by water vapor errors in radiosondes [Jackson and Gasiewski, 1995]. A synopsis of activities undertaken during the period from July 1, 1994 to June 30, 1996 follows.

1. MIR Data Processing. Nine-channel radiometric imagery has been obtained using the MIR on the NASA ER-2 during the Convection and Moisture Experiment (CAMEX September-October, 1993 and CAMEX2, August-September, 1995), the Tropical Ocean Global Atmosphere/Coupled Ocean-Atmosphere Response Experiment (TOGA/COARE, January-March 1993), and related aircraft deployments. A key task in this investigation has been the optimal calibration, archiving, and interpretation of the multichannel imagery. Progress has been made in the first and last of these tasks (calibration and interpretation). Data archiving is currently underway, and has been delayed pending final calibration.

Calibration of radiometric data from instruments such as the MIR has been most commonly accomplished using a linear infinite impulse response (IIR) filter operating on single-scan gain and offset estimates. While this method is quick it does not properly filter the large spurious gain and offset jumps and spikes that can impair the interpretation of the radiometric data. Moreover, the time constant and order of the IIR filter are often chosen by qualitative guess. In order to account for nonstationary features such as jumps and spikes and to provide the optimal form for the gain and offset calibration filter, a nonlinear multidimensional Wiener filter was developed for radiometer calibration [Sharpe et al., 1995]. The filter first searches for nonstationary jumps and spikes in the raw (single-scan) gain and offset data, then removes them. Jump heights are estimated and stored in a table; spikes are replaced by a local moving average. The resulting gain and offset stream consists of stationary data. A joint gain/offset (2-dimensional) Wiener filter is subsequently constructed using autocorrelation estimates of the gain and offset processes. After filtering, the gain and offset jumps are replaced at their original locations.

The performance of the Wiener filter can be judged by analyzing the variance of MIR clear-air brightness temperature fluctuations for calibration both with the Wiener filter and with a standard IIR filter (Figure 1). In the clear-air case the brightness fluctuations are primarily caused by

instrumental rather than geophysical noise. The instrumental noise consists of radiometric integration noise and calibration noise. As shown in Figure 1, the total noise decreases significantly when the Wiener filter is used. Although the precise degree of calibration noise reduction depends on the channel, improvements of several decibels are possible.

The calibrated MIR imagery has been displayed and analyzed using subroutines developed for use within the computational environment MATLAB. The MATLAB environment allows extensive image analysis using simple interactive matrix commands. Typical MIR imagery over isolated oceanic convective precipitation cells are shown in Figure 2. Baseline brightness temperatures were subtracted so that only brightness temperature perturbations are shown. As can be seen, the high-spatial resolution SMMW channels clearly map the extent of small convective precipitation cells. Moreover, saturation within the cell center (as occurs in infrared imagery over precipitation cells) is absent and the change in brightness is monotonic. For these same cells, the 89-GHz channel provides a weak non-monotonic response that only shows the small region within the core of the cell. It is believed that many such small cells are completely missed when estimating rain from spaceborne instruments since the sensor footprint averages over both bright and dark regions of the cell top. The monotonicity and high available spatial resolution of the SMMW channels is a distinct advantage in cell mapping. Since the time-integral of cell area is statistically related to total rainfall volume, the SMMW channels are thus potentially very useful for indirect rainfall estimation.

In order to gauge the information content of the storm-core imagery, Karhunen-Loève (KL) transforms of the brightness temperature perturbations imagery were performed over selected channel subsets. In order to account for expected changes in brightness statistics as a function of the beam scan angle, several KL transforms were computed for small ranges of incident angle. In this manner, a KL transform appropriate for the incident angle of each pixel was applied. The transformed imagery for the MIR window channels at 150, 220, and 325 ± 9 GHz show decorrelation but not complete statistical independence. In order to further decompose the KL channels, a nonlinear transformation based on a third-order regression was applied. The resulting three channels exhibited excellent statistical independence (Figure 3). As can be seen in the resulting nonlinear-KL imagery significantly different storm cell structure can be seen in the transformed window-channel imagery. The first image shows gross depressions in the brightness spectrum caused by ice scattering; the second image shows a map related nonlinearly to the tilt (or slope) in the brightness temperature spectrum. For many regions of the map the second image exhibits entirely different structure than the first. It is believed that the second image is related to particle size and ice canopy thickness.

The TOGA/COARE and CAMEX aircraft flights included the NASA Marshall Space Flight Center's Advanced Microwave Precipitation Radiometer (AMPR). The AMPR and MIR provide nearly complementary data sets in that the AMPR channels cover the lower-frequency microwave window channels at 10.7, 18.7, 37.0 and 89.0 GHz. An amalgamation of AMPR and MIR data has been performed for the overflight of cyclone Oliver on February 8, 1993 (Figure 4). The amalgamated imagery clearly illustrates the absorption signature of rain at the 10.7 and 18.7 GHz channels and a progressively increasing scattering signature at higher frequencies. Interestingly, the eyewall radius of the cyclone as delineated by the 10.7, 18.7, and 37.0 GHz channels is smaller (by ~30%) than the radius of any eyewall-related brightness structure observed in the higher-frequency

imagery. Apparently, the 89-GHz and higher-frequency channels respond primarily to clouds above the eyewall rain layers, and delineate a “false eyewall.” The false eyewall is well-centered around the “rain eyewall,” but larger in radius. The meteorological nature of the false eyewall and of the fine-structure observed within it in the 89-GHz channel are a subject of current research. An understanding of these features will facilitate proper interpretation of future high-resolution multispectral aircraft and satellite imagery.

Pixel-by-pixel comparisons of the MIR and AMPR brightness temperatures at the common channel of 89 GHz indicate that the AMPR measurements are biased ~3K warmer than the MIR brightness temperatures. The standard deviation of the brightness temperature difference between the two instruments is ~2K over a ~35K range of variation. This figure is comparable to the root sum square of the noise temperatures of each individual instrument, thus indicating good consistency between the instruments.

2. Nonlinear Iterative Statistical Retrievals of Precipitation Parameters. Although the SMMW and SMMW channels above ~220 GHz have the ability to image with high spatial resolution, they do not penetrate as deeply through clouds and rain cells as lower frequency channels. The inherent tradeoff between penetration depth and spatial resolution requires the application of both spatial and spectral raincell statistics in precipitation parameter retrieval algorithms. The ability to retrieve cloud and precipitation parameters using SMMW imagery depends to a great extent on statistical relationships between the various low-level precipitation parameters (e.g., surface rain rate) and the ice and water burden in the cloud top. In an effort to more fully exploit the information content in both SMMW and lower frequency microwave imagery a nonlinear iterative statistical technique based on the CLEAN algorithm [Thompson et al., 1991] was developed. The algorithm retrieves rain rate (RR) and integrated ice content (IIC) using noisy multiresolution multispectral brightness temperature imagery.

The algorithm begins with a single-step estimation of RR from the observed microwave imagery using the nonlinear statistical retrieval algorithm described by Skofronick and Gasiewski [1995]. Hydrometeor profiles are estimated from these retrieved values using a statistical stormcell mode. A forward radiative transfer and antenna pattern convolution algorithm subsequently operates on these profiles to produce predicted multiresolution multispectral imagery. The predicted imagery is subtracted from the observed imagery to produce residual imagery. As in the radioastronomical version of CLEAN, the algorithm locates a peak in the norm of the residual imagery, then adds a small statistically-determined amount of both precipitation parameters (RR and IIC) to the unknown geophysical parameter field. New brightness imagery, including the effects of antenna pattern convolution, are re-computed via the forward radiative transfer algorithm, and the residual imagery is updated. A new search for the residual peak is initiated, and the algorithm repeats.

The utility of this algorithm is currently being investigated using one-dimensional cuts of simulated multichannel brightness temperature imagery of a convective tropical squall. The hydrometeor data is taken from the NASA/GSFC Goddard Cumulus Ensemble (GCE) data set, and the channels are those of the EOS MIMR, albeit nadir viewing. The forward radiative transfer model described by Gasiewski and Staelin [1990] was used in both generating the simulated MIMR imagery and performing the forward radiative transfer calculations within the iterative retrieval algorithm. Figure

2 shows rain rate truth and retrieved rain rate for a one-dimensional cut through the GCE. Retrieved rain rates using the iterative CLEAN-based algorithm (dotted curve) are compared to those obtained using the single-step nonlinear statistical retrieval algorithm. Some error reduction is noted, particularly at the edges of the cell where the impact of a broad antenna beam would tend to cause overestimation. Further development of this algorithm including means of incorporating spatial statistics of the hydrometeor parameter field and application to SMMW imagery is warranted.

3. Simulated Neural Net Retrievals of Precipitation Parameters. The retrieval of precipitation parameters from noisy multispectral imagery can be facilitated using the nonlinear statistical mapping capability of feed-forward neural nets. The utility of neural nets was shown by Spina et al. [1994, 1995] for the retrieval of cell top altitude from 118-GHz aircraft data from the Millimeter-wave Temperature Sounder. To extend the use of neural net algorithms to spaceborne systems, neural net retrievals of precipitation parameters using simulated multiband spatially-filtered MIMR imagery were performed and compared to retrievals using a nonlinear statistical method [Gasiewski et al., 1996, see Appendix A]. Net training is accomplished using the backpropagation algorithm along with appropriate degrees of momentum and adaptive learning. With proper training, the neural nets consistently outperform conventional nonlinear statistical techniques in single-pixel retrievals.

The neural net technique developed here has been used to study the tradeoffs associated with using various microwave channel sets and sensor resolutions. For example, rain rate (RR) and integrated ice content (IIC) retrieval accuracies are displayed in Figures 3 and 4 for a variety of MIMR channel sets (see Table 1). The results illustrate that area-averaged RR retrieval accuracy suffers considerably from resolution degradation, while IIC requires essentially only the 37 and 89 GHz channels. Moreover, the case of purely an 89-GHz channel (case #6) suggests that RR retrieval accuracy can actually be improved (slightly) through resolution degradation. While this case might at first seem counterintuitive, it is believed to show the importance of using morphological features of the imagery to improve retrieval accuracy, in this instance by simply averaging over adjacent pixels. Significant improvements in RR and IIC retrieval accuracies are expected to be gained through proper use of precipitation cell morphology.

4. SMMW Probing Depth Calculations During 1995 and 1996 the PI participated in working group meetings in support of a Geosynchronous Microwave Sounder (GMS) definition study. The GMS working group meetings have been an interagency (NASA and NOAA) forum to define a concept for a high-resolution geosynchronous sounding and imaging satellite using submillimeter wave channels. The GMS is the first the first geosynchronous sounder to utilize a small aperture antenna (1-2 m diameter) along with 325, 380, and 410 GHz sounding channels.¹

In support of the GMS study the PI has performed probing height calculations illustrating the depth into the atmosphere that can be probed by various sounding channels (Figure 5-7). The calculations used the Liebe 1987 water vapor and oxygen absorption model [Liebe, 1987] within the Georgia Tech Microwave Radiative Transfer (MRT) code, assuming clear air. This height is limited by screening from water vapor in the lower and middle troposphere and hence varies considerably with latitude and season. Due to strong continuum absorption around the SMMW absorption lines, the

¹ A report by the GMS working group is to be drafted and published in early 1997.

probing height in the summer tropical and sub-tropical latitudes is limited to 3-5 km from the surface. Direct probing of clouds, precipitation, water vapor, and temperature are possible above this altitude, while only indirect (or statistical) probing is possible below.

5. The Boulder Atmospheric Observatory Experiment (BAOEX). During February of 1995 a comprehensive field experiment to measure atmospheric thermal emission over a wide range of frequencies was performed. The experiment was conducted at the Boulder Atmospheric Observatory site at 40.05° N, 105.00° W, and 1577 m MSL. The site and time of year were chosen so as to provide atmospheric conditions characterized by relatively little vertically-integrated moisture (< 5 mm), thus resulting in SMMW brightness temperatures cold enough to be used for meaningful comparisons with RT models.

The following suite of instruments was assembled: (1) the MIR, operating in upward scanning mode, (2) a zenith-looking Fourier-transform infrared spectrometer, (3) a Vaissala optical cloud ceilometer, (4) special radiosonde launches, (5) a 23.83 and 31.65 GHz zenith-looking water vapor and cloud radiometer, and (6) meteorological tower measurements of temperature, pressure, and humidity from the surface to 300 m altitude. The purpose of BAOEX was to characterize thermal emission of the clear atmosphere over a broad range of the spectrum from centimeter wavelengths to the infrared. The high-altitude site was chosen to provide partial atmospheric transparency at SMMW frequencies so that meaningful brightness temperature intercomparisons could be made. Data are being analyzed with the goal of improving the continuum absorption model for frequencies near 325 GHz.

6. Upgrade of the MIR 325-GHz Receiver. A new 325-GHz receiver was purchased jointly by Georgia Tech and NASA/GSFC in 1995. The receiver consists of a 325-GHz mixer and 162-GHz local oscillator (LO). The new receiver is expected to be received from the ZAX Millimeter Wave Corporation, San Dimas CA, by December, 1996, and is expected to provide a significantly lower system noise temperature (~1200 K) than the existing 325-GHz receiver (~3000 K). A lower noise temperature is critical in being able to perform proper absolute calibration of the MIR SMMW channels. The new receiver will use a second-harmonic mixer/LO design to provide complete RF rejection of all sub-bands lying below 325 GHz but above the cutoff frequency of the 325-GHz feedhorn. Pending success in the fabrication of this receiver, the development of a receiver at 424 GHz for SMMW temperature sounding will be considered.

7. Definition of a Low-cost SMMW Space Sensor. In response to the University Space Research Association's Student Exploration and Development Initiative (STEDI) an Earth science mission incorporating a low-cost polar-orbiting MMW/SMMW imaging sensor was proposed.² The High-resolution Submillimeter- and Millimeter wave Imaging Radiometer (HSMIR) includes channels at 118, 183, and 325 GHz and would fly at ~350 km altitude. The applications of this sensor include:

² "Study and Measurement of Global Water Vapor, Cloud Ice, Temperature and Precipitation using the High Resolution Submillimeter/Millimeter-Wave Imaging Radiometer (HSMIR)," proposal to the Universities Space Research Association Student Exploration and Development Initiative (STEDI), A.J. Gasiewski, P.G. Steffes, G.L. Stephens, D.H. Staelin, and J.R. Wang, submitted August 1994.

- Studying the global distribution and structure of cirrus ice clouds and upper tropospheric water vapor with 2 km pixel resolution (5 km 3-dB resolution) over a full seasonal cycle.
- Demonstrating high-resolution global profiling of water vapor using radiometric measurements near the 183.310 GHz water vapor resonance.
- Demonstrating for the first time high-resolution global profiling of atmospheric temperature and estimation of cell top altitude using radiometric measurements near the 118.750 GHz oxygen resonance.
- Exploring the capability of water vapor profiling at 325.153 GHz. Such techniques would have potential important application from geosynchronous orbit (see 4 above).
- Studying the structure of frozen hydrometeors associated with convective storms using radiometric channels spanning over an octave bandwidth. Additional observable modes are expected to provide unique information on hydrometeor size distributions.

Unique attributes of this sensor include a Nyquist spatial resolution of 2 km at the highest frequency channel and polarimetric sensitivity at the scan extremes. Further development in the areas of space-qualified SMMW receiver technology and MMW/SMMW retrieval algorithms are warranted to reduce mission risk and improve scientific product.

8. Coupled-Wave Electromagnetic Scattering Model. An improved model for computing the bistatic scattering characteristics of an absorbing wedge-corrugated periodic structure (e.g., of the type used for radiometer calibration) has been developed. The model uses the linear multiport coupled-wave method described by Gasiewski and Jackson [1994, 1995] and scattering matrix composition by slab doubling. The routine is written in MATLAB and can be easily executed on a 100 MHz PC. Calculations of normal-incidence reflectivity for a structure with varying period Λ and for several depths d are illustrated in Figure 8. The dimensions are normalized to the electrical wavelength λ . The assumed dielectric parameters are $\epsilon=9-j0.4$ and $\mu=1-j0.5$; these are typical of iron-loaded epoxy absorber material. It is noted that these calculations are for the total load reflectivity, and thus include power scattered into all possible Floquet harmonics. In order to complete the investigation of the one-dimensionally periodic absorber case, improved measurements of the bistatic scattering characteristics of a wedge-corrugated absorbing load sample have been undertaken.³

³ The measurements are being performed at the University of Washington, Seattle WA, in conjunction with Professor Y. Kuga's experimental studies in rough surface scattering.

CONCLUSIONS AND RECOMMENDATIONS

The following conclusions and recommendations are provided regarding the studies undertaken during the period from July 1, 1994 through June 30, 1996.

1. Radiative transfer model verification using data from TOGA/COARE, CAMEX, and BAOEX will be continued during 1997. Recently purchased processing equipment includes a 80586 PC with 2 GB hard drive, providing enough memory and processing speed to accommodate the MIR data. Due to their slow operating speed and cumbersome and unreliable software, Exabyte tape drives will be phased out for data storage and archiving. Rather, a write-once CD ROM drive will be procured for archiving the MIR CAMEX, TOGA/COARE, and BAOEX data. The CD-ROM will provide much quicker and more universal access to this data, and will thus facilitate distribution to collaborating parties. Both level-1 (raw) data and level-2 (calibrated imagery) data will be archived to facilitate distribution and analysis. The multidimensional Wiener filter provides improved calibration accuracy and will be adopted during all processing of level-2 data.
2. The nonlinear iterative method of parameter estimation is a potentially useful technique for optimally using multiresolution passive microwave imagery to estimate precipitation parameters. The method is based on a well-known technique used in radioastronomy for image deconvolution (the CLEAN algorithm), but extended to accommodate multiple radiometric channels, a nonlinear relationship between the observed imagery and the underlying geophysical parameter field, and statistics of the geophysical parameter field. The algorithm is currently being tested on one-dimensional line plots of brightness temperatures computed using MRT applied to the GCE squall data. Convergence of the algorithm in its current test state is unacceptably slow. The slow convergence is believed to be attributed (in part) to an insufficient number of degrees of freedom in the retrieved parameter field. Currently, only two parameters (surface rain rate and integrated ice content) are used, however, other parameters such as ice particle size affect the brightness temperature significantly (especially at short wavelengths), and thus should be included in the parameter set. In addition, the use of two-dimensional brightness data (i.e., maps) is expected to improve convergence by providing additional spatial information.
3. Neural net precipitation cell parameter retrievals from simulated microwave brightness temperature imagery offer the possibility of both improving the retrieval accuracy and reducing the retrieval computation time from any precipitation parameters. The nonlinear multidimensional mapping capability of neural nets is particularly well suited to the inverse problem in passive remote sensing. During the upcoming year the neural net technique will be applied to simulated SMMW brightness temperature imagery to establish relationships between SMMW brightness temperatures and the underlying rain rate in convective cumulonimbus clouds.

Further development of this algorithm including means of incorporating spatial statistics of the hydrometeor parameter field and application to SMMW imagery is warranted. Accordingly, neural net precipitation cell parameter retrievals from simulated SMMW imagery using precipitation cell morphological information will be investigated. The use of spatial information (readily available in cell imagery of the type obtainable from a LEO SMMW satellite) will be studied by augmenting the GCE data base with statistically generated cloud fields using a synthetic cloud simulator. In this

manner, a large ensemble of cells will be available for use in training the net to recognize typical cell features. The Georgia Tech Microwave Radiative Transfer (MRT) model, suitably modified to accommodate cirrus anvil ice at submillimeter-wave frequencies, will be used to generate brightness fields for use in neural net training and retrieval studies.

4. Questions regarding the use of SMMW channels mostly center around the probing depth that these channels can attain. Important related questions are the precise degree of the continuum absorption near the SMMW lines, and the bulk absorption and scattering coefficients of cloud ice and liquid distributions at SMMW frequencies. As a consequence of the limited probing depth for both clear air and clouds, the relationship of SMMW brightness temperature perturbations to low-altitude precipitation rate and integrated ice density is at best statistical. Determination of this statistical relationship is central to the use of SMMW data to improve estimates of rain rate (and hence, latent heat transfer in convective cells) and ice content (and hence, cell-top albedo estimates). To this end, further amalgamation of aircraft data from the AMPR, Millimeter-wave Temperature Sounder, and MIR instruments will be performed in order to provide wideband data sets for MMW and SMMW RT model verification.

Two additional meetings of the GMS working group will be held within the upcoming year to address these questions. To support these activities, the PI will attend each of these meetings. In addition, to make the Georgia Tech MRT code more available to scientists involved in SMMW propagation research, the code will be ported to a PC and/or UNIX platform. The availability on these systems should provide for more widespread use and distribution.

5. The BAOEX data is expected to provide a good means of corroborating clear-air radiative transfer models near the 325-GHz SMMW absorption line. However, the development of purely- or partly-physical retrieval techniques for cloud and raincell parameters require improvements in SMMW radiative transfer modeling within clouds and precipitation. Accordingly, a ground-based experiment focussing on combined active MMW sensing, lidar sensing, and passive MMW/SMMW imaging for the purpose of radiative transfer modeling in clouds will be organized to take place in either late 1997 or early 1998. The experiments will be a follow-on to the Boulder Atmospheric Observatory (BAO) experiments of February 1995, but will concentrate more heavily on obtaining data in hydrometeor-laden atmospheres for the purpose of MMW and SMMW radiative transfer modeling. The work will be carried out using the NASA/GSFC MIR, the Georgia Tech Polarimetric Scanning Radiometer (PSR) and instruments provided by the NOAA Environmental Technology Laboratory in Boulder, CO. A dry high-altitude site such as the BAO site will be sought for the experiments so as to reduce the water vapor continuum absorption within the submillimeter-wave bands to appropriate levels for study.

6. Improvements in the sensitivity of the MIR 325-GHz SMMW receiver are absolutely necessary to advancements in retrieval accuracy and RT modeling at SMMW frequencies. In addition, the fabrication of new receivers at additional SMMW bands (e.g, 380.197 and 424.763 GHz) are suggested to further explore the capabilities of high-resolution cloud sensing, and water vapor and temperature sounding. Accordingly, a new 325-GHz receiver being fabricated by the ZAX Millimeter Wave Corporation will be installed in the MIR and tested during 1997, pending delivery by ZAX. The PI will support data processing and field experiments using the MIR during flights

occurring in 1997 using the new 325-GHz receiver.

7. The HSMIR design study demonstrated that a relatively low-cost spaceborne SMMW sounder could be developed from (with the exception of the SMMW receivers) mostly from off-the-shelf components. The sensor would provide particularly high spatial resolution, and thus would be a good candidate for synoptic rain cell mapping and high-resolution temperature and water vapor sounding. The SMMW channels would also be significantly more sensitive to integrated ice content of cirrus clouds, and thus provide a potentially new method of observing global cloud ice content. Cloud cover is a significant feedback mechanism in global climate models, and current models are in relatively poor agreement as to the amount of cloud cover that would accompany a given temperature rise. Thus, the establishment of a global cloud content data base using, e.g., a SMMW imaging sensor of the HSMIR-class is an important practical goal. Accordingly, the development of radiative transfer models in cloud ice and IIC retrieval algorithms using SMMW data will be given high priority in the upcoming year.

8. While RT modeling and retrieval development using SMMW channels is the primary emphasis of this investigation, practical airborne and spaceborne SMMW sensors require absolute calibration to within 0.5 K accuracy. An improved understanding of the emission characteristics of wedge- and pyramid-shaped blackbody targets is one of several key issues in this problem. (Other issues include near-field antenna pattern knowledge, antenna main beam efficiency, local oscillator reflections from calibration loads and other sidelobe-illuminated structures, and calibration load thermal gradients.) The coupled-wave technique has been shown to be able to predict the scattering characteristics of wedge-shaped targets well. Extensions of this technique to the pyramid-shaped structure are expected to yield a computationally efficient tool for studying and optimizing the more practical (unpolarized) blackbody target. Of equal importance is knowledge of the thermal distribution within the target, which can be addressed through improved thermal modeling.

SENSOR TRADE-OFF BRIGHTNESS TEMPERATURE CHANNEL COMBINATIONS

Case #	Channel (GHz)					
	6.0	10.67	18.7	23.8	36.5	89.0
1	X					
2		X				
3			X			
4				X		
5					X	
6						X
7		X	X			
8			X		X	
9					X	X
10			X	X	X	
11		X	X		X	
12			X		X	X
13			X	X	X	X
14		X	X	X	X	X
15	X		X	X	X	X
16	X	X		X	X	X
17	X	X	X		X	X
18	X	X	X	X		X
19	X	X	X	X	X	
20	X	X	X	X	X	X
21*	X	X	X	X	X	X

*Case #21 used a neural net with six hidden nodes; all other cases used four nodes.

Table 1. MIMR channels sets used in the neural net simulated retrieval studies. Nadir observations are assumed.

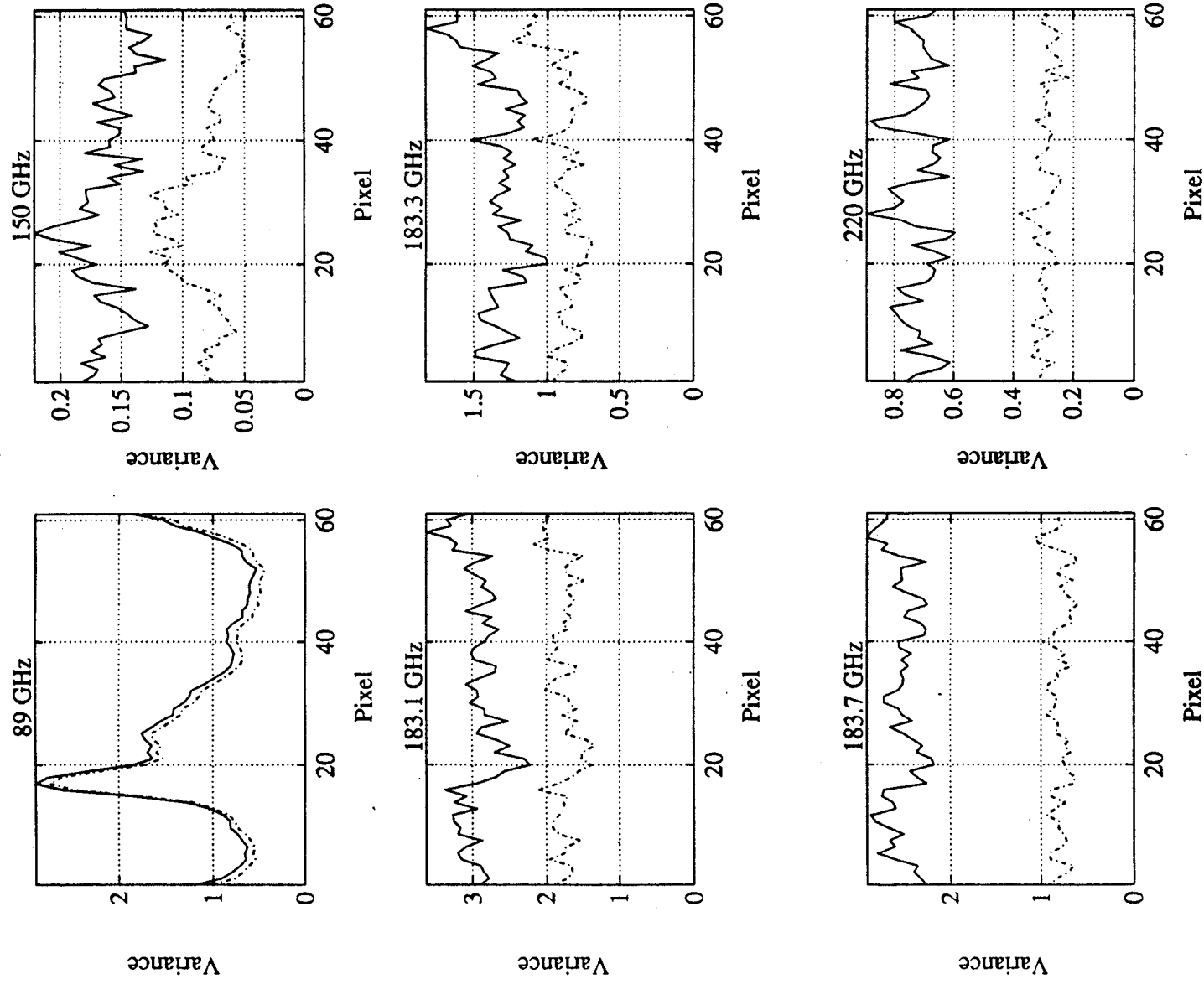


Figure 1. Along-track average values of MIR clear-air brightness temperatures obtained using a conventional IIR calibration filter (solid lines) and optimal Wiener filter with spurious jump and impulse detection (dashed lines). A significant reduction in calibration noise is apparent in several channels.

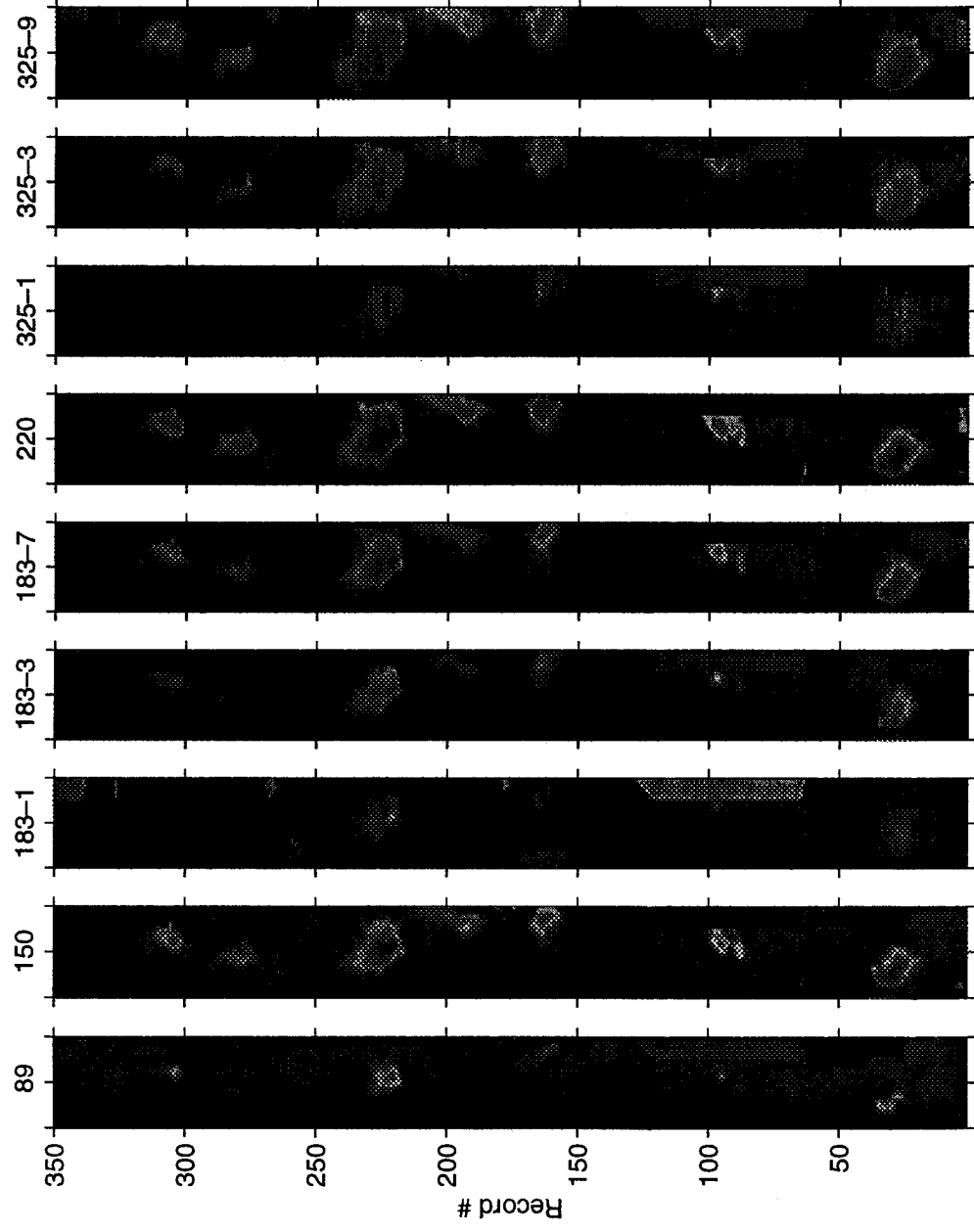


Figure 2. MIR convective cell brightness temperature perturbation imagery. The imagery illustrates the rain cell mapping capability of SMMW channels. A flight line of ~210 km length is shown.

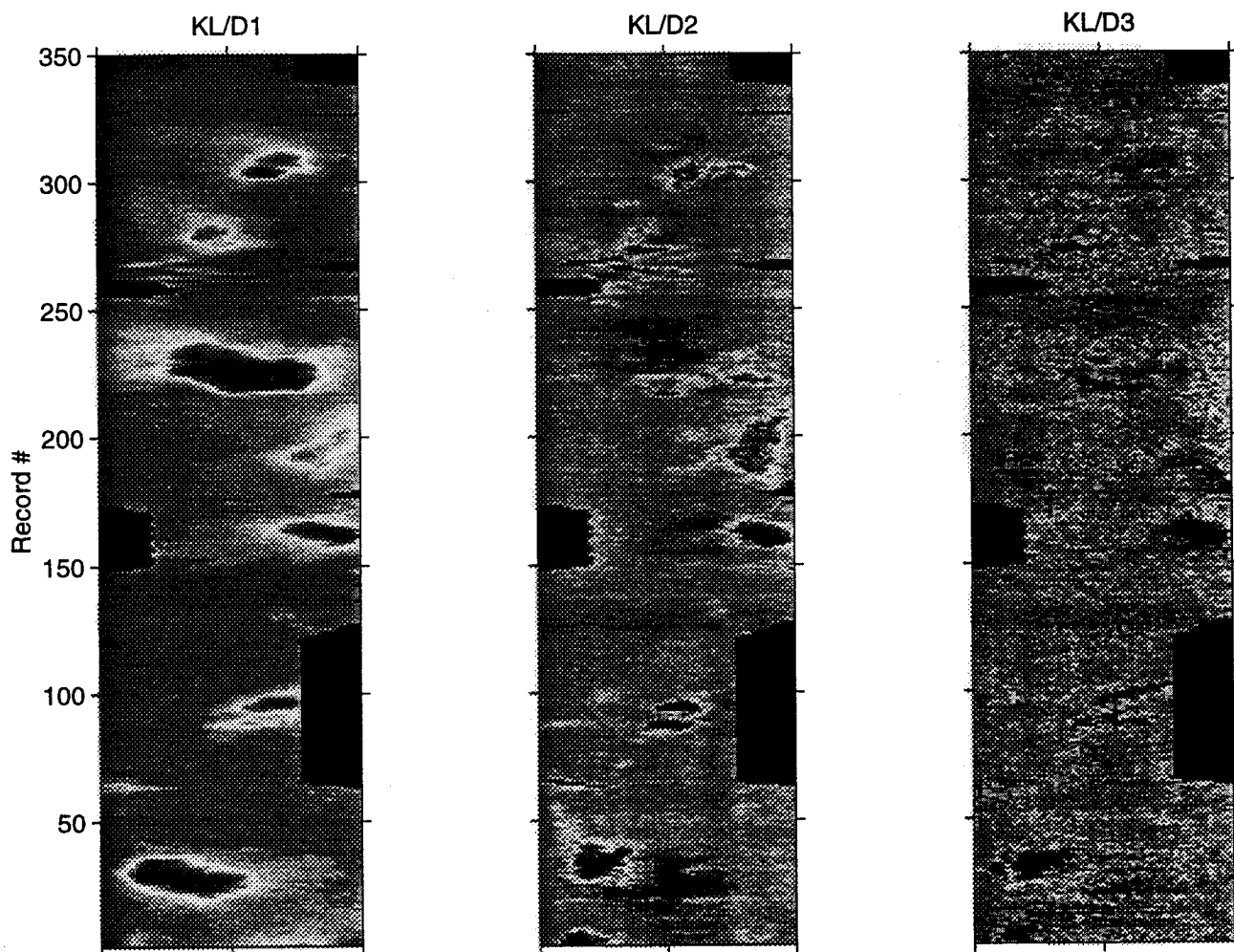


Figure 3. Nonlinearly-transformed Karhunen-Loève brightness imagery based on three-channel (150, 220, and 325 ± 9 GHz) MIR imagery. At least two independent channels with high signal-to-noise ratios are observed.

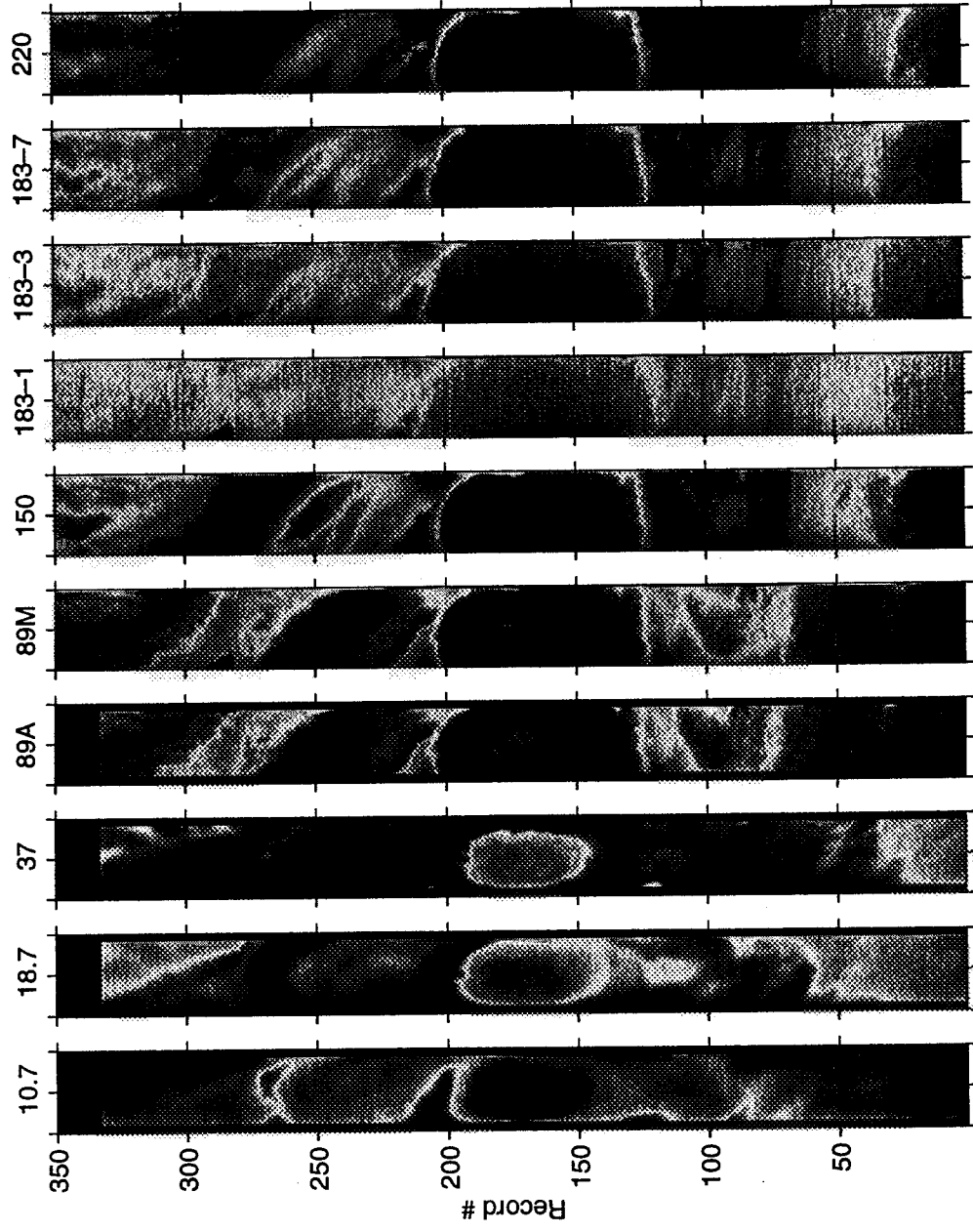


Figure 4. Amalgamation of AMPR and MIR imagery for ER-2 overflights of cyclone Oliver on February 8, 1993. A flight line of ~210 km length is shown.

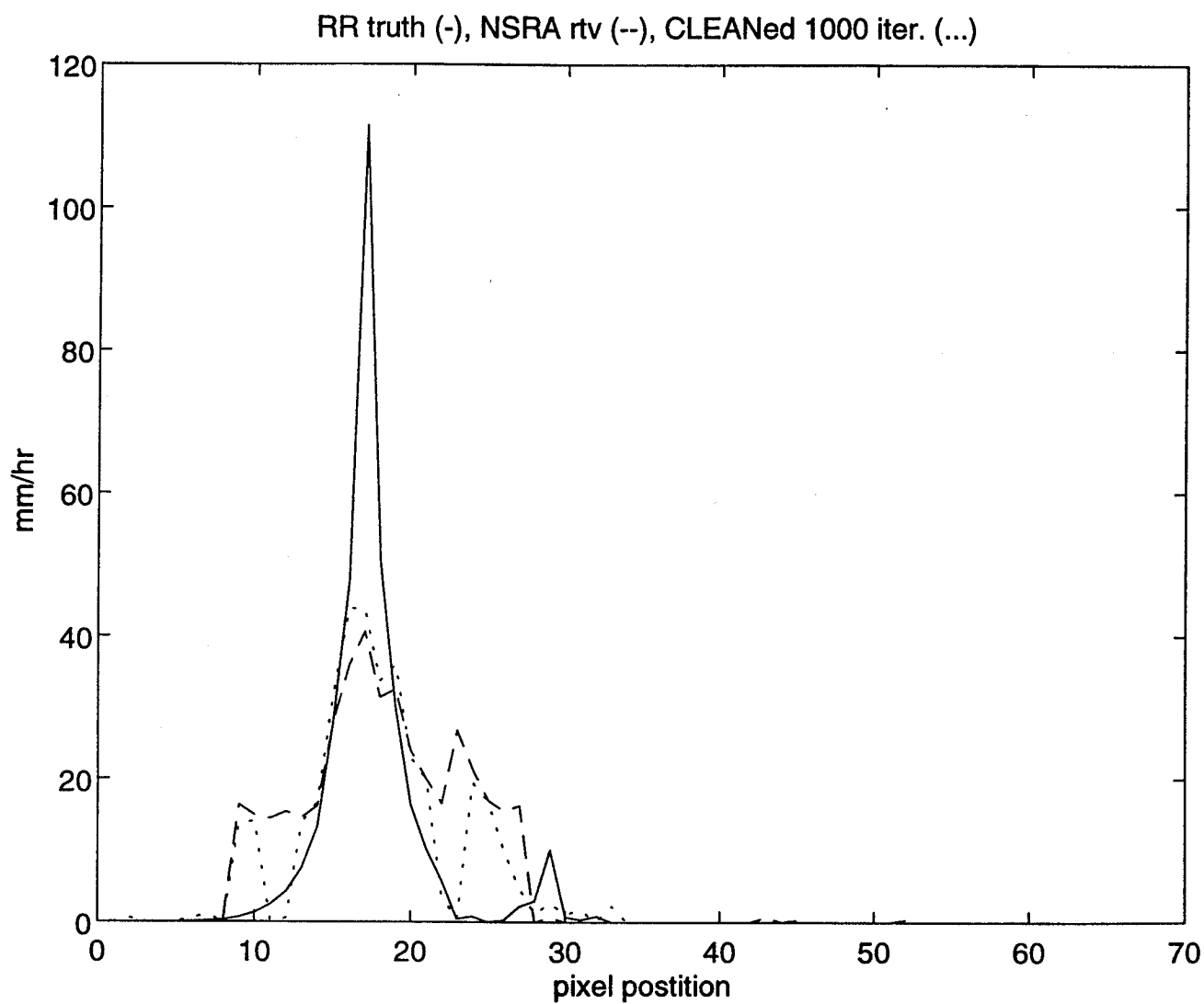


Figure 5. Rain rate truth (solid curve) and retrieved rain rate in mm/hr for a one-dimensional cut through the NASA/GSFC Goddard Cumulus Ensemble data set. Retrieved rain rates used the nonlinear statical retrieval algorithm (dashed curve, [Skofronick and Gasiewski, 1995]) and the iterative statistical CLEAN algorithm (dotted curve) described in the text.

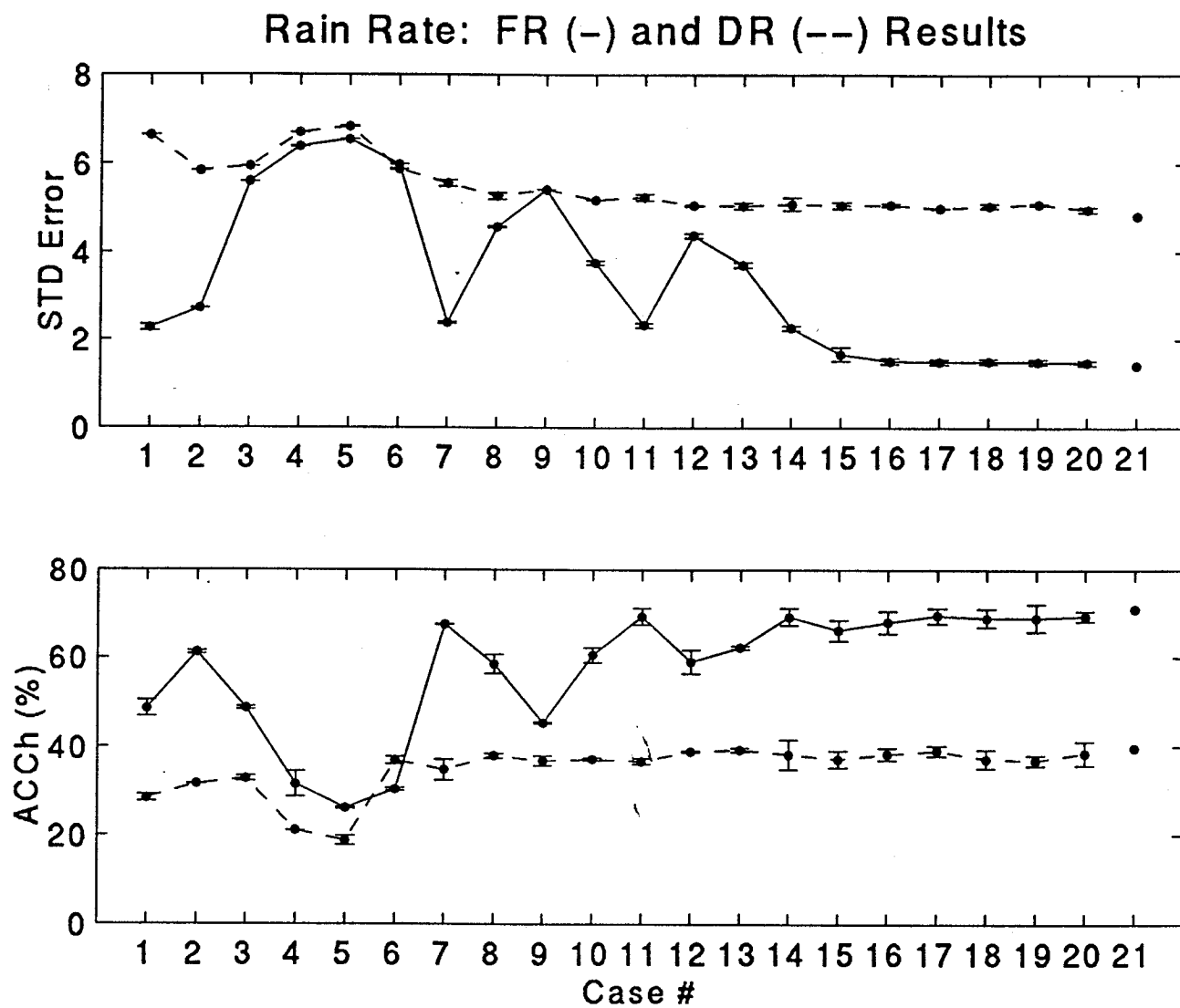


Figure 6. Full resolution (FR) and degraded resolution (DR) rain rate retrieval errors for various MIMR channel sets. Both error standard deviation and hybrid accuracy (see Appendix A) are shown.

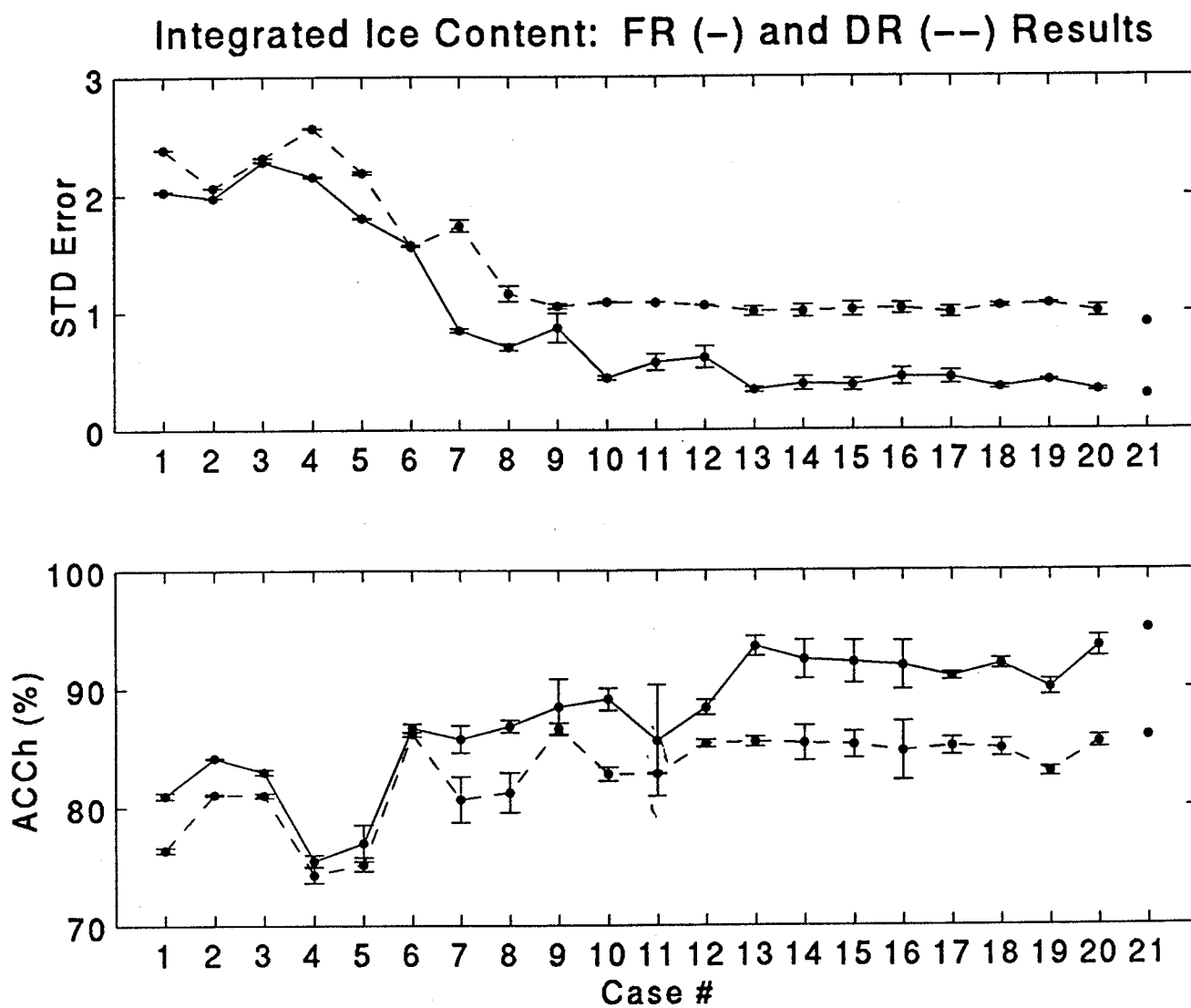


Figure 7. Full resolution (FR) and degraded resolution (DR) integrated ice content retrieval errors for various MIMR channel sets. Both error standard deviation and hybrid accuracy (see Appendix A) are shown.

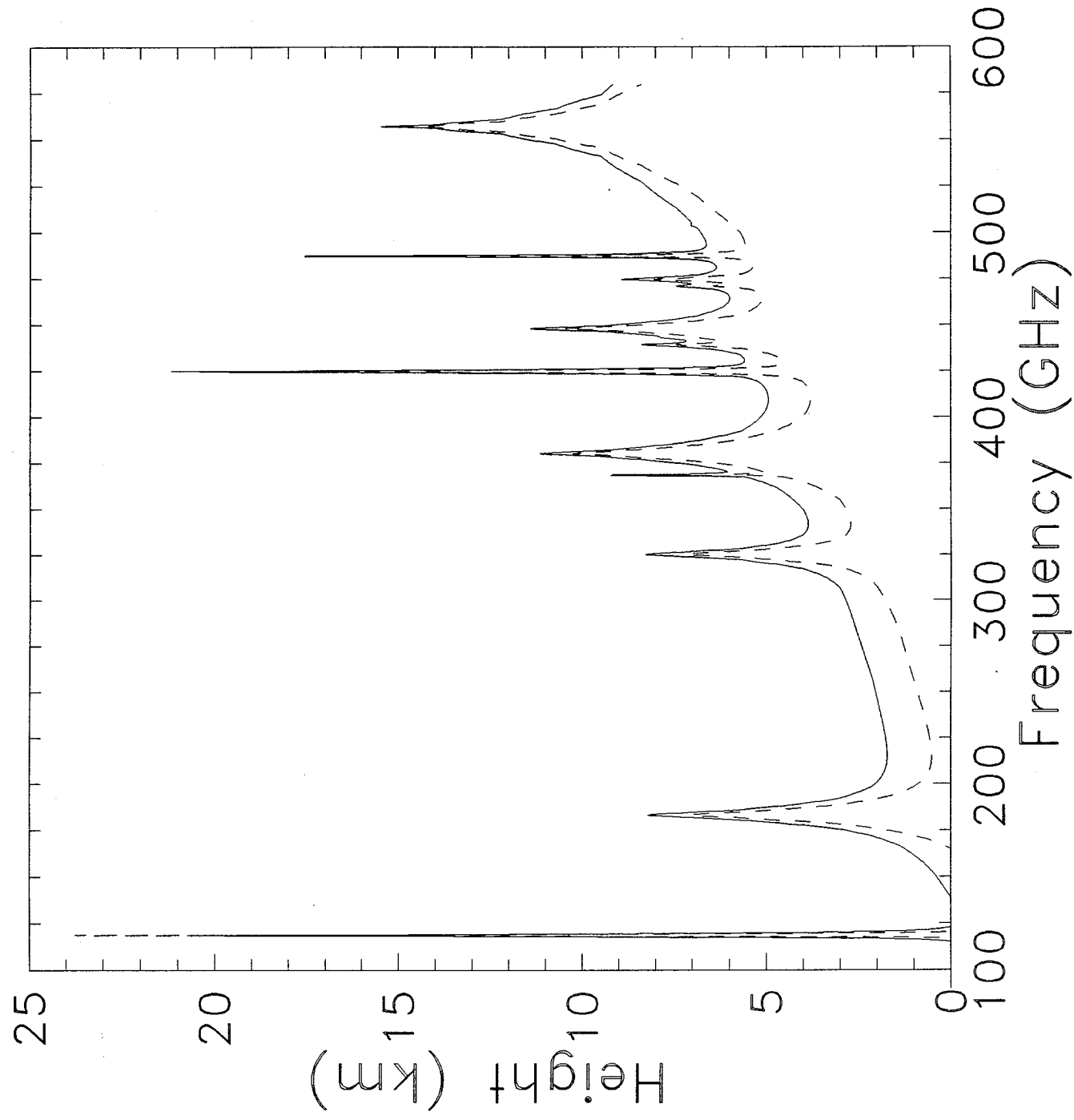


Figure 8. Nadir probing heights of millimeter- and submillimeter-wave channels for tropical latitudes (0° - 30°) and standard summer conditions. Plots for one (solid) and two (dashed) optical depths are shown.

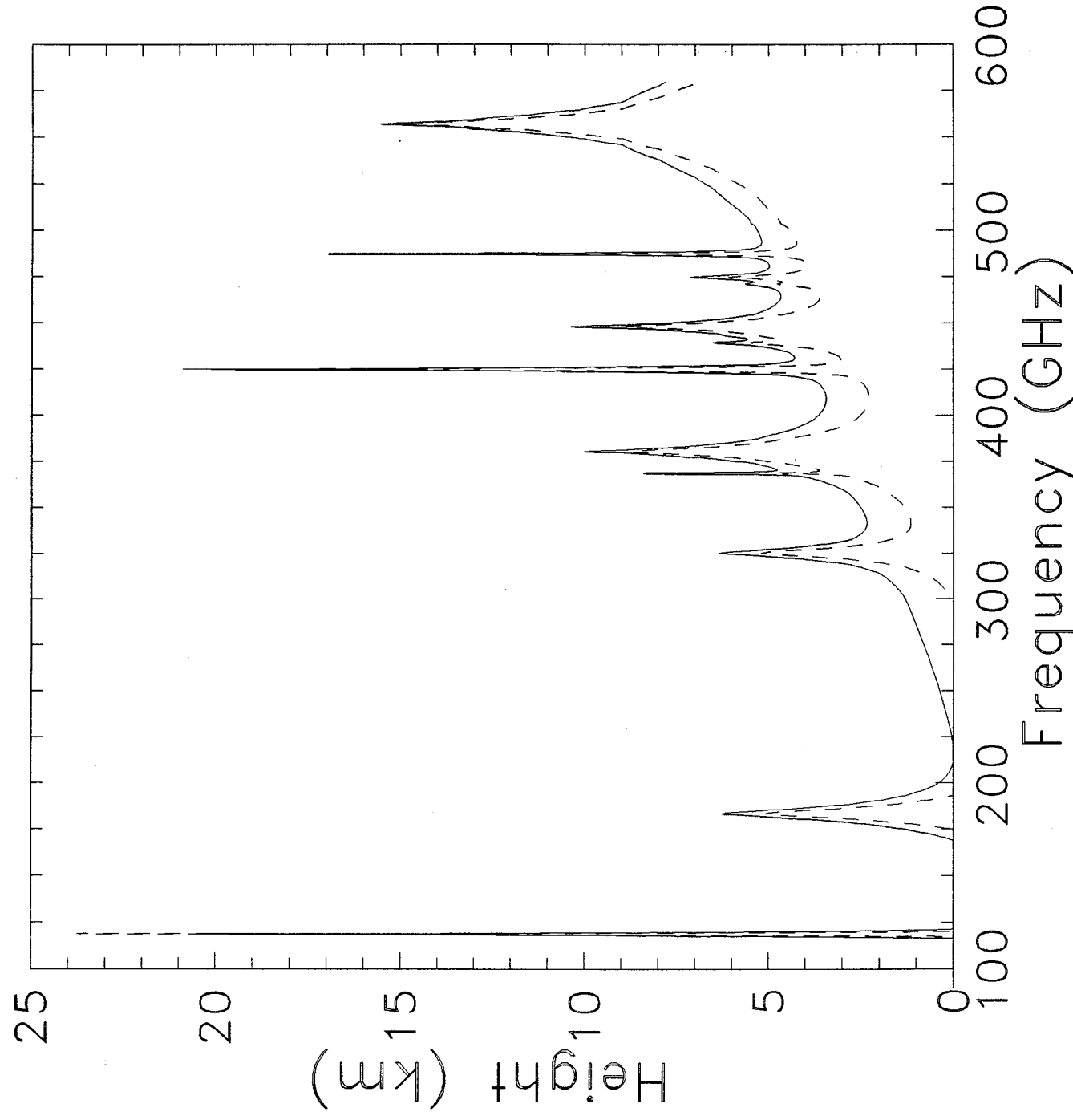


Figure 9. Nadir probing heights of millimeter- and submillimeter-wave channels for middle latitudes (30°-60°) and standard annual conditions. Plots for one (solid) and two (dashed) optical depths are shown.

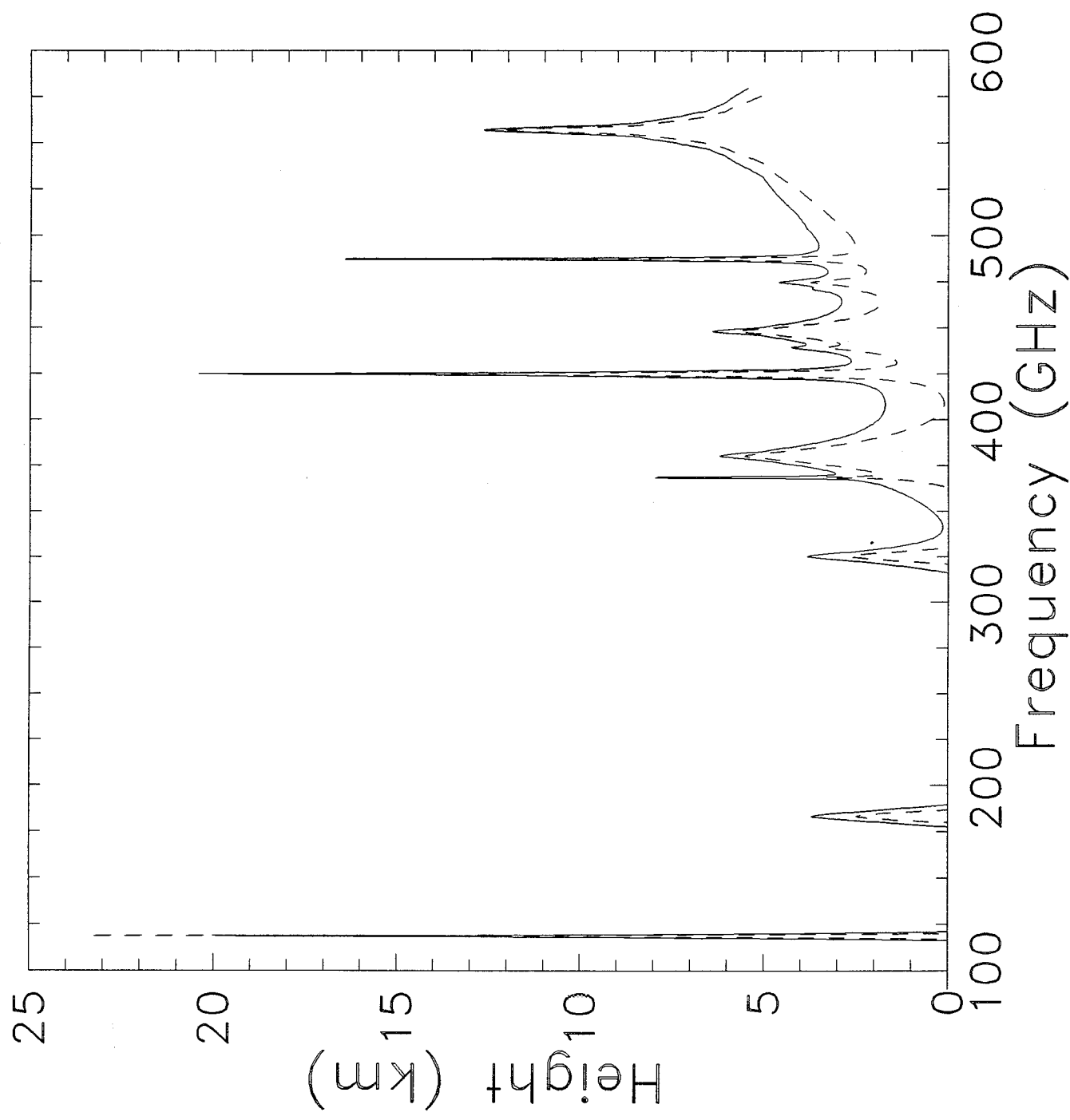


Figure 10. Nadir probing heights of millimeter- and submillimeter-wave channels for polar latitudes (60°-90°) and standard winter conditions. Plots for one (solid) and two (dashed) optical depths are shown.

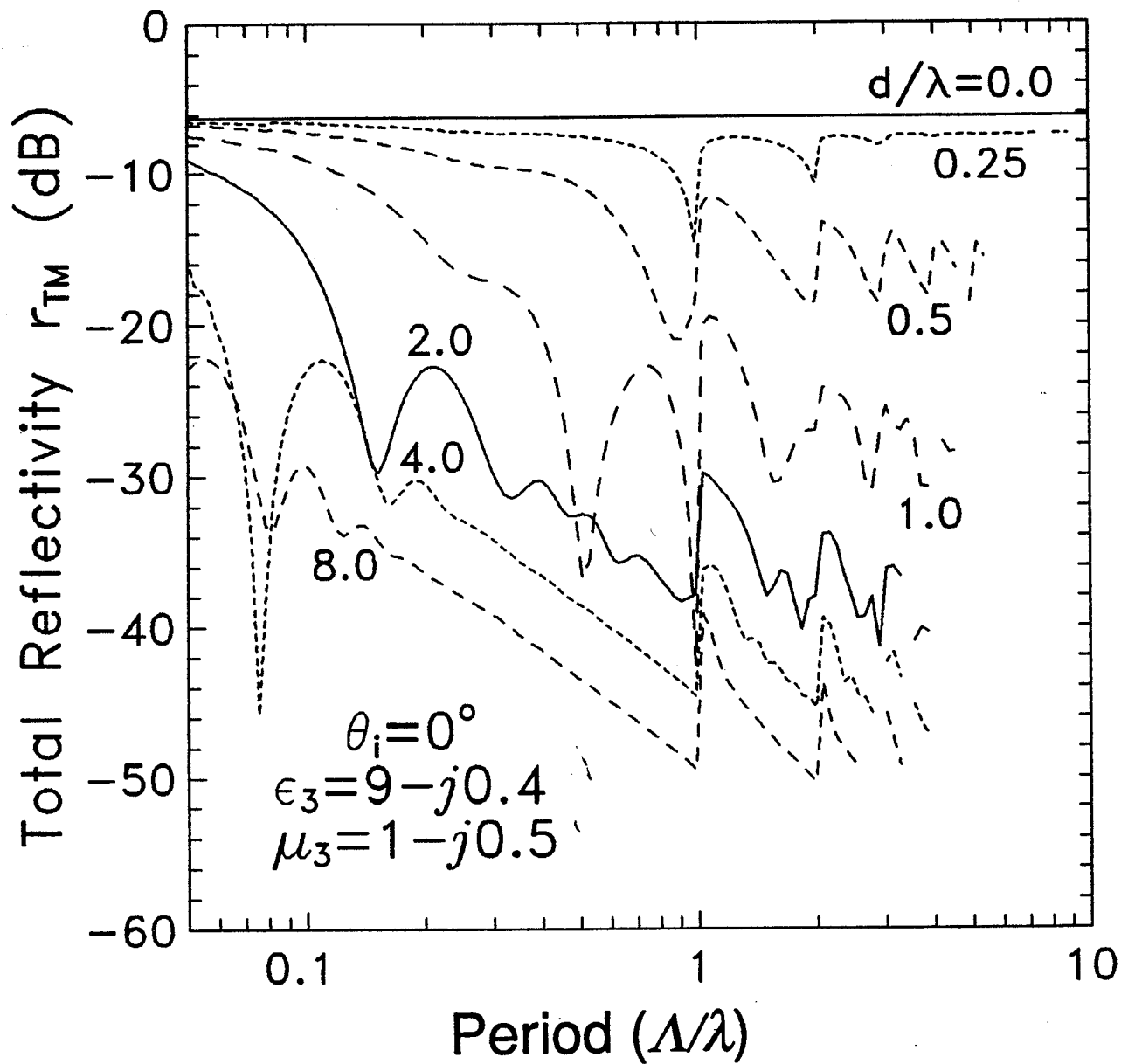


Figure 11. Normal-incidence total TM reflectivity for a wedge-corrugated absorbing calibration load. The wedge period is Λ and the depth is d . These dimensions are normalized to the electrical wavelength λ .

REFERENCES

- Gasiewski, A.J. and Staelin, D.H., "Numerical Analysis of Passive Microwave O₂ Observations Over Precipitation," *Radio Science*, vol. 25, no. 3, pp. 217-235, May-June 1990.
- Gasiewski, A.J., Jackson, D.M., Wang, J.R., Racette, P.E., and Zacharias, D.S., "Airborne Imaging of Tropospheric Emission at Millimeter and Submillimeter Wavelengths," *Proceedings of the 1994 International Geoscience and Remote Sensing Symposium*, vol. 2, pp. 663-665, presented at the California Institute of Technology, Pasadena, CA, August 8-12, 1994.
- Gasiewski, A.J. and Jackson, D.M., "Electromagnetic Scattering from Lossy Periodic Surfaces: Application to Microwave Absorbers," submitted to *IEEE Trans. Ant. Propagat.*, March 1993; revised, October 1994.
- Gasiewski, A.J., and Jackson, D.M., "Coupled-Wave Linear Multiport Solution for Plane Wave Scattering from Periodic Structures and Interfaces," *Proceedings of the 1995 Progress in Electromagnetics Research Symposium (PIERS)*, p. 463, presented at the University of Washington, Seattle, WA, July 24-28, 1995.
- Gasiewski, A.J., Showman, G.A., and Skofronick, G.M., "Application of Neural Nets to Rain Rate Retrieval from Simulated Multichannel Passive Microwave Imagery," *Proceedings of the 1996 International Geoscience and Remote Sensing Symposium*, pp. 1688-1691, presented in Lincoln, NE, May 27-31, 1996.
- Jackson, D.M. and Gasiewski, A.J., "Millimeter-Wave Radiometric Observations of the Troposphere: A Comparison of Measurements and Calculations based on Radiosonde and Raman Lidar," *IEEE Trans. Geosci. Remote Sensing*, vol. 33, no.1, pp. 3-14, January 1995.
- Liebe, H.J., "A Contribution to Modeling Atmospheric Millimeter-wave Properties," *Frequenz*, vol. 41, pp. 31-36, 1987.
- Racette, P.E., Adler, R.F., Wang, J.R., Gasiewski, A.J., Jackson, D.M., and Zacharias, D.S., "An Airborne Millimeter-Wave Imaging Radiometer for Cloud, Precipitation, and Atmospheric Water Vapor Studies," *J. Atmos. Oceanic Tech.*, vol. 13, no. 3, pp. 610- 619, June, 1996.
- Sharpe, S.J., Gasiewski, A.J., and Jackson, D.M., "Optimal Calibration of Radiometers Using a Multi-dimensional Gain-Offset Wiener Filter," *Proceedings of the 1995 Progress in Electromagnetics Research Symposium (PIERS)*, p. 729, presented at the University of Washington, Seattle, WA, July 24-28, 1995.
- Skofronick-Jackson, G.M. and Gasiewski, A.J., "Nonlinear Statistical Retrievals of Ice Content and Rain Rate Using Passive Microwave Observations of a Simulated Convective Storm," *IEEE Trans. Geosci. Remote Sensing*, vol. 33, no. 4, pp. 957-970, July, 1995.
- Spina, M.S., Schwartz, M.J., Staelin, D.H., and Gasiewski, A.J., "Images of Convective Cell-Top

Altitudes Using 118-GHz Spectral Data," *Proceedings of the 1994 International Geoscience and Remote Sensing Symposium*, vol. 4, pp. 1870-1872, presented at the California Institute of Technology, Pasadena, CA, August 8-12, 1994.

Spina, M.S., Schwartz, M.J., Staelin, D.H., and Gasiewski, A.J., "Application of Multilayer Feedforward Neural Networks to Precipitation Cell-Top Altitude Estimation," submitted to *IEEE Trans. Geosci. Remote Sensing*, January 1995.

Thompson, A.R., J.M. Moran, and G.W. Swenson, *Interferometry and Synthesis in Radio Astronomy*, Malabar, FL: Krieger Publishing Co., 1991.

Application of Neural Nets to Rain Rate Retrieval from Simulated Multichannel Passive Microwave Imagery

A.J. Gasiewski, G.A. Showman, and G.M. Skofronick

School of Electrical and Computer Engineering
Georgia Institute of Technology, Atlanta, GA 30332-0250
(404) 894-2984; (404) 894-2934; FAX (404) 894-4641

ag14@prism.gatech.edu ; gt7418d@prism.gatech.edu ; gail@cem1.ee.gatech.edu

Abstract - The retrieval of precipitation parameters from passive microwave imagery requires the use of a nonlinear statistical estimation technique operating on a multichannel data stream. We describe here the application of a feed-forward neural net to the estimation of precipitation parameters from noisy, multispectral brightness temperature imagery. A comparison of the neural net retrieval technique vis-à-vis a nonlinear statistical technique shows that with proper training the neural net achieves slightly better performance. The neural net technique developed here has been used to study the tradeoffs associated with using various microwave channel sets and sensor resolutions. Initial calculations using simulated nadir-viewing imagery for a MIMR-compatible set of six channels are presented.

1. INTRODUCTION

Nonlinear retrieval techniques using either model-based iteration or supervised high-order curve fitting have been shown to be useful for precipitation parameter retrieval (e.g., [1]). Recently, neural nets have seen increasing use in remote sensing studies as classifiers and (to a lesser extent) as continuous parameter retrieval operators. The advantages of neural nets for the latter application include the ability to capture relevant high-order statistical information in the underlying data set and the capability to form highly nonlinear multidimensional mapping functions. These are both essential attributes for many geophysical sensing problems. In addition, neural nets exhibit flexibility in adding weakly correlated information from additional sources [2] and are simple to implement. While a review of neural nets for parameter estimation is beyond the scope of this paper, a sufficient background is developed in [3, 4, 5].

We report here the development of a neural network technique appropriate for rain rate (RR) retrieval using multichannel passive microwave brightness imagery at 6.0, 10.7, 18.7, 23.8, 36.5, and 89.0 GHz. The imagery was computed using the Georgia Tech Microwave Radiative

Transfer (MRT) model [6] for five time values of the Goddard Cumulus Ensemble (GCE) microphysical stormcell model [7] over an ocean background. Two spatial resolutions were used in this study: (1) full resolution (FR) imagery consisting of 64 x 64 pixels sampled on a 1.5 km grid, and (2) degraded-resolution (DR) imagery consistent with the imaging capabilities of a diffraction-limited aperture antenna of diameter 1.6 m at 705 km altitude. DR imagery was obtained by convolving the FR imagery with the gain pattern of a circular antenna with quadratic field amplitude taper (Figure 1). Pseudorandom Gaussian noise appropriate for the observation geometry and scan rate were added to the convolved imagery to simulate the radiometric imaging process.

Brightness imagery sampled at five storm temporal stages (126, 138, 174, 210, and 234 minutes) were used, thus providing a total of 20,480 multispectral pixels. The data set was identical to that used in [1]. Training and test sets of equal size were derived from this set by pseudorandom partitioning.

2. NETWORK ARCHITECTURE AND TRAINING

Two-layer (i.e., one hidden layer) neural nets were trained on the MRT/GCE data using a variety of node numbers (from two to eight), training algorithms, weight initialization, and input prefiltering methods. The hidden layer perceptrons used the hyperbolic-tangent sigmoid as their activation transfer function, while the single perceptron of the output layer used a pure-linear transfer function. Both Karhunen-Loève (KL) and non-KL prefiltering was used.

The nets were implemented using the MATLAB Neural Net Toolbox backpropagation software which allows the option of using an adaptive learning rate (ALR) and momentum term in the training rule. Together ALR and momentum facilitate net training by increasing the likelihood of escaping shallow local minima in error space while rapidly traversing regions characterized by relatively gradual error descent slopes. These features reduced training and test RMS errors by 20-30% for a fixed number of training epochs. In order to negotiate the deep er-

ror troughs encountered in the error landscape, an adaptive hard-limit (ALR-AH) algorithm was developed. The salient feature of this modification is an adaptive limit on the maximum value of the learning rate.

Both uniform pseudo-random and Nguyen-Widrow initialization of the net weights and biases were studied. Net performance did not appear to be affected by the type of initialization. Nets were trained until RMS training errors stabilized; nets with six nodes in the hidden-layer were typically trained for 3000 epochs, and nets with 4 nodes for 2000 epochs. These limits reflect good compromises between complete convergence and reasonable training times. Since nets that are trained on the same data but randomly initialized will inevitably result in differing final weights and RMS errors, an ensemble of nets were trained for the case studies described below. Training of the net using the KL modes of the input data was also tested. Using only the highest energy modes for training and testing offers the possibility of reducing net complexity without compromising retrieval performance.

3. NEURAL NET RETRIEVAL PERFORMANCE

To compare the retrieval performance of a neural net to that of the nonlinear statistical retrieval (NSR) algorithm in [1], a number of nets with four and six hidden nodes were trained on the entire ensemble of data, i.e., without partitioning. The nets were trained with both brightness temperature and KL-transformed data. The retrieval performance of nets using KL data was comparable to nets trained with brightness temperatures. However, the training on KL data occasionally resulted in nets with very large RMS errors. Similarly poor performance were not observed for any of the nets using brightness temperatures, thus, brightness temperature-based retrievals are used in the comparison.

The results for retrievals of RR and integrated ice content (IIC) at both full and degraded resolution using the NSR algorithm and neural net are summarized in Table 1 (see also Figures 2a and b). The better of the KL or brightness temperature (BT) retrievals from [1] appear in the table. The retrieval performance of 6-node nets was slightly better than for the 4-node nets. However, the 4-node nets have approximately the same number of degrees of freedom as does the NSR algorithm, so these results are used in the comparison.

The first measure of performance in the table is the standard deviation of the retrieval error. The second is unconstrained accuracy (a_u), defined as the percentage of pixels with retrieval errors less than 1.0 mm/hr RR or 0.5 kg/m² IIC. The final measure is a constrained accuracy (a_c), and is the same as a_u , except that only those pixels

with true RR greater than 0.01 mm/hr or IIC greater than 0.001 kg/m² are included in the calculations. The neural nets always have a smaller error standard deviation, and in three of the four cases have higher values of a_u and a_c .

Table 1. Rain rate (RR) and integrated ice content (IIC) retrieval performance comparisons between a nonlinear statistical and neural net algorithm.

RR	FR		DR (1.6m)	
	NSR(BT)	NN(4-node)	NSR(KL)	NN(4-node)
σ_e (mm/hr)	1.93	1.63	6.20	5.33
a_u (%)	90.7	92.5	88.9	88.6
a_c (%)	46.2	56.2	36.6	35.6
IIC	NSR(BT)	NN(4-node)	NSR(KL)	NN(4-node)
	σ_e (kg/m ²)	0.91	0.34	1.36
	a_u (%)	92.2	94.5	90.4
	a_c (%)	87.2	90.1	84.2

4. SENSOR TRADEOFF SIMULATION

The neural net retrieval operator was used to study the tradeoffs in rain rate retrieval accuracy for specific channel sets and sensor resolutions. To this end, equal-size training and test data sets were created by pseudo-random partitioning of the entire five-frame data set. Figure 3 shows plots of the standard deviation of the net output error and a_c for FR and DR 4-node RR retrievals. The abscissa indicates the particular channel case: 0 denotes the use of all 6 channels, 1 denotes the use of only the 6.0 GHz channel, etc., 6 denotes the use of only the 89 GHz channel. Retrieval performance on the training set is shown with solid lines, and test set with dashed lines. The error bars reflect the use of two realizations for each condition to provide a measure of the simulation noise inherent in the use of neural nets.

Using only the 6.0 GHz channel results in a FR retrieval error not too much greater than those achieved by the nets trained on all channels. The worst retrieval is obtained using the 36.5 GHz channel alone, a consequence of the bimodal nature of the brightness variations over oceanic convection for this channel. The 6.0- and 10.67 GHz channels are the most useful in the FR single-channel case. For the DR case, the most useful channel is at a higher frequency (e.g., 18.7 or 89 GHz). This conclusion is expected since the higher frequency channels provide better spatial resolution, and hence better accuracy at any given pixel.

The training rate on a 100 MHz 486 computer for a net with 6 hidden nodes and training on all of the available data (20480 pixels with 6 brightness temperatures each) was about six seconds per epoch; machine usage was approximately six million flops per epoch. In general

the training time and total operation count were found to scale well to the number of hidden nodes and the size of the training set and weakly with the number of input channels or modes, as expected from complexity calculations.

5. SUMMARY

Feedforward multilayer neural nets were trained on brightness temperatures from simulated brightness images of a tropical convective storm. Data was available for five stages of the storm's development. The nets were trained to retrieve rain-rate (RR) and integrated ice content (IIC) using the backpropagation algorithm. The retrieval performance of these nets was compared to that of a nonlinear statistical retrieval algorithm. The results suggest that the neural net estimators will be at least as accurate in precipitation parameter retrieval as conventional nonlinear statistical methods, and that KL pre-filtering can potentially improve net performance. Neural net retrieval operators were also used to determine the importance of individual single radiometric channels and sensor spatial resolution to rain rate retrieval accuracy. The reduced spatial resolution available when observing with low-frequency microwave channels in low-Earth orbit (i.e., 6.0 and 10.7 GHz) makes these channels significantly less useful for precipitation parameter retrieval than certain higher frequency channels (e.g., 18.7 and 89 GHz).

Acknowledgments: The authors would like to thank M. Homiller and J. Piepmeier for their assistance with the computer hardware and software.

REFERENCES

- [1] G.M. Skofronick-Jackson and A.J. Gasiewski, "Non-linear statistical retrievals of ice content and rain rate from passive microwave observations of a simulated convective storm", *IEEE Trans. Geosci. Remote Sensing*, vol. 33, no. 4, pp. 957-969, July 1995.
- [2] M.S. Spina, M.J. Schwartz, D.H. Staelin, and A.J. Gasiewski, "Application of multilayer feedforward neural networks to precipitation cell-top altitude estimation", in *Proceedings of the 1994 International Geoscience and Remote Sensing Symposium (IGARSS)*, Pasadena, CA, 1994, vol. 4, pp. 1870-1872.
- [3] R. P. Lippmann, "An introduction to computing with neural nets", *IEEE ASSP Magazine*, April 1987.
- [4] B. Widrow and M. A. Lehr, "30 years of adaptive neural networks: Perceptron, madaline, and backpropagation", *Proc. IEEE*, vol. 78, no. 9, pp. 1415-1440, 1990.
- [5] R. Beale and T. Jackson, *Neural Computing: An Introduction*, Adam Hilger, New York, 1990.
- [6] A.J. Gasiewski and D.H. Staelin, "Numerical analysis of passive microwave O₂ observations over precipitation", *Radio Science*, vol. 25, no. 3, pp. 217-235, May-June 1990.
- [7] R.F. Adler, H.-Y.M. Yeh, N. Prasad, W.K. Tao, and J. Simpson, "Microwave simulations of a tropical rainfall system with a three-dimensional cloud model", *J. Clim. Appl. Met.*, vol. 30, pp. 924-953, 1991.

FIGURES

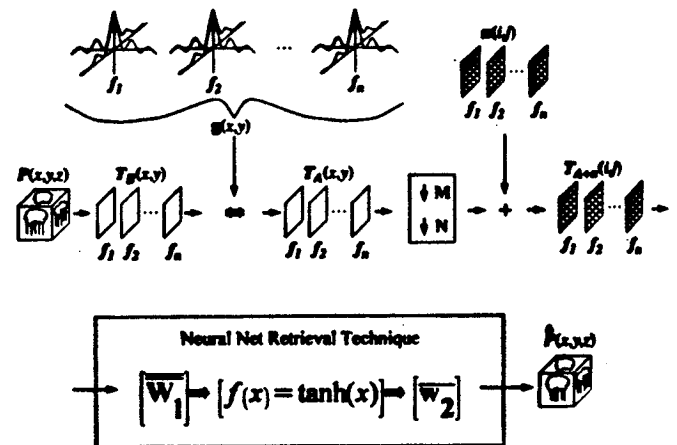


Figure 1: Block diagram of the passive microwave simulation and retrieval process. The neural net estimator was used in the retrieval stage.

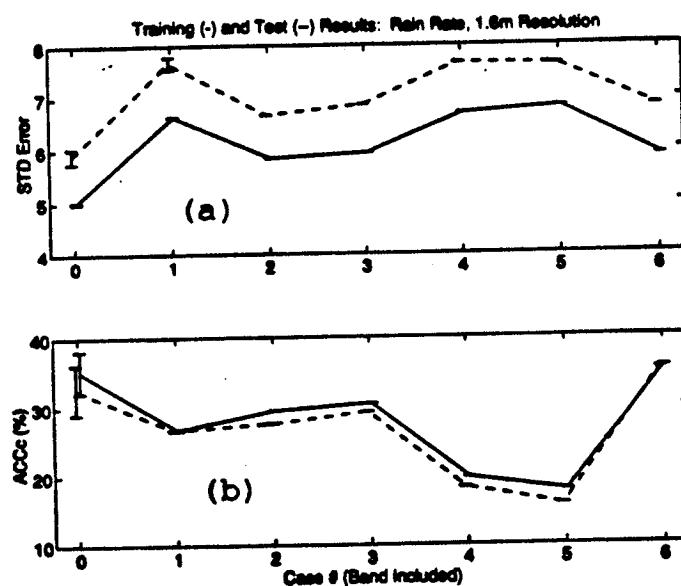
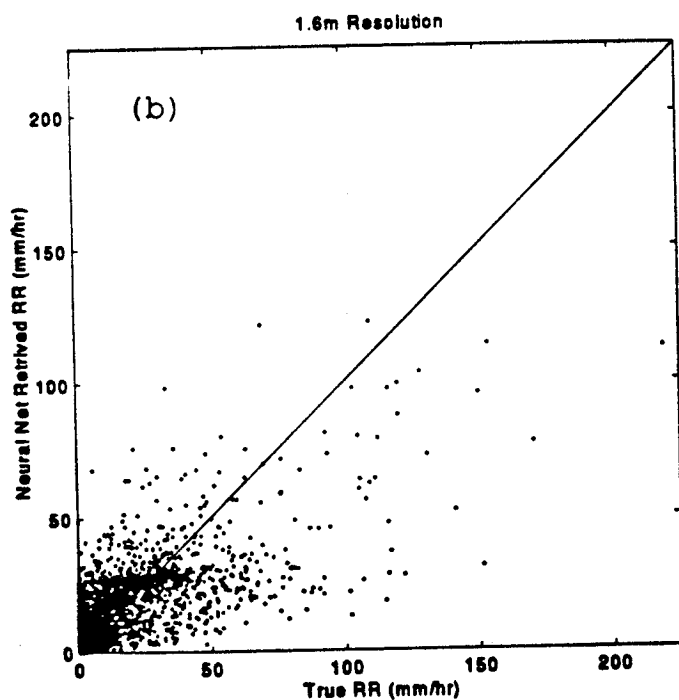
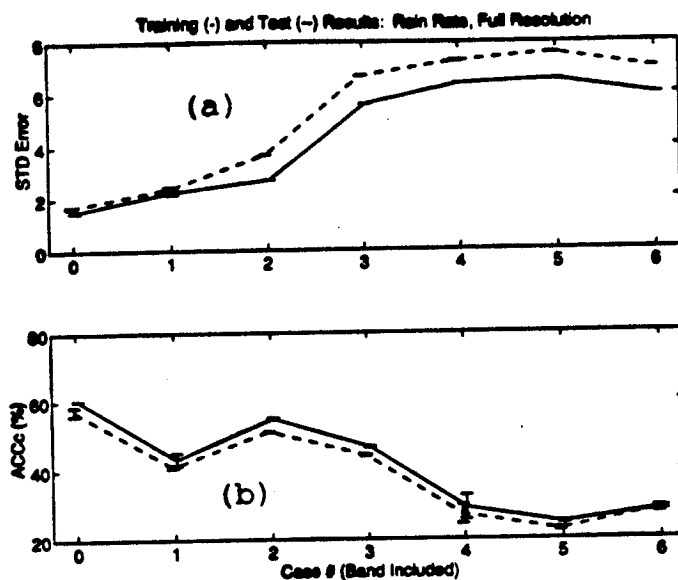
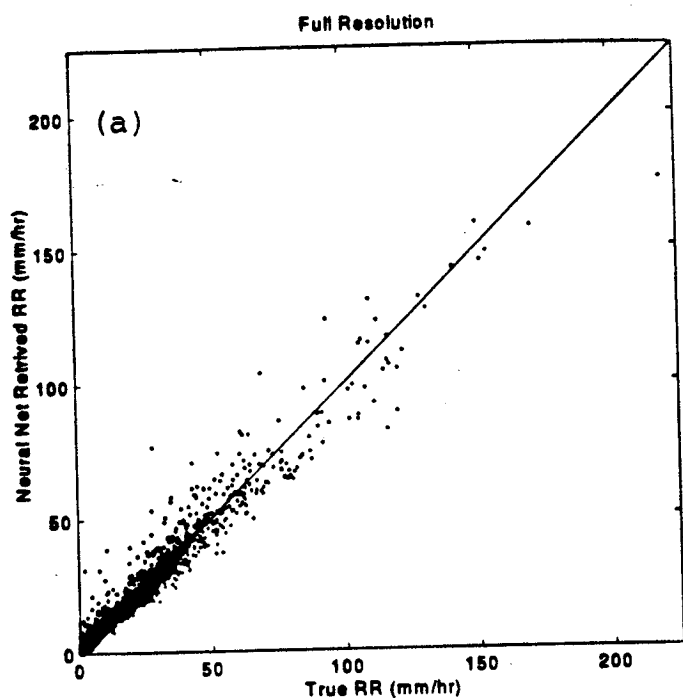


Figure 2: Scatter plot of rain rate retrieved from (a) FR imagery and (b) DR imagery using a six node neural net and six radiometric channels (6.0, 10.7, 18.7, 23.8, 36.5, and 89.0 GHz).

Figure 3: Plots of the (a) standard deviation of the net output error and (b) constrained accuracy a_c for FR and DR (1.6m) neural net rain rate retrieval. A 4-node net was used.